

Water Quality Algorithms

By: ASU Carbon Mapper Land and Ocean Team

Version 1.0

1. Algorithm Description

1.1. Objective

The objective of the Water Quality (WQ) algorithms is computation of the concentrations of chlorophyll *a* (Chl, $\mu\text{g/L}$) and suspended particulate matter (SPM, mg/L), and the absorption coefficient of colored dissolved organic matter at a reference wavelength of 440 nm (CDOM, m^{-1}) from imaging spectroscopy data. The algorithms should be transferable to different regions.

1.2 Theoretical Background

The color of natural waters results from the interaction of light with water molecules, organic and inorganic materials that are dissolved or suspended in it, and in shallow and clear enough waters, materials at the bottom of the water column. Equations that describe how these components modify water color are called bio-optical models. Such models can be used to quantify the abundance of those materials interacting with light from measurements of optical properties such as reflectance.

Optical properties can be classified into inherent optical properties (IOPs) that solely depend on the material, and apparent optical properties (AOPs) which also depend on illumination, such as remote sensing reflectance, which is commonly used in aquatic remote sensing (R_{rs} , sr^{-1}):

$$R_{rs}(\lambda) = \frac{L_w(\lambda)}{E_d(\lambda)} \quad (1)$$

where L_w is the water-leaving radiance ($\text{W m}^{-2} \text{nm}^{-1} \text{sr}^{-1}$), E_d is the downwelling plain irradiance ($\text{W m}^{-2} \text{nm}^{-1}$), and λ indicates wavelength.

The materials in the water column that interact with light—referred to as optically active constituents—can be operationally categorized into pools of phytoplankton, SPM, and CDOM. Phytoplankton and CDOM primarily affect absorption whereas SPM primarily affects scattering.

Phytoplankton abundance is typically quantified as the concentration of Chl *a*, which is the main light harvesting pigment used for photosynthesis present in all photoautotrophic plants and bacteria. Chl *a* concentration can be inferred from light absorption and scattering through mass-specific spectral coefficients, which differ between phytoplankton types due to variations such as pigment composition, cell structure, growth conditions, and physiology (Bricaud et al. 2004). See Section 1.3.1.1 for more details.

SPM, also referred to as total suspended solids or total suspended material, is operationally defined as material with a diameter greater than a 0.7 μm , which includes many phytoplankton and bacteria as well as non-algal particles (NAP) like suspended sediments and other detritus. Concentrations can be inferred through mass-specific spectral coefficients, which vary greatly depending on origin, size distribution, and mineral composition of particles (Stramski et al 2007). See Section 1.3.1.2 for more details.

CDOM, also known as yellow substance, gelbstoff, or gilvin, is the optically active portion of dissolved organic matter and is operationally defined as material that passes through a sub-micron filter (e.g. 0.2 μm). This chemical mixture includes byproducts from the breakdown of both terrestrial and aquatic plant matter such as humic and fulvic acids, whose chromophores have absorption peaks in the UV. Although optical properties of CDOM vary according to its origin, biological and photochemical degradation, and environmental conditions, its abundance can be approximated using an exponential function that represents the longwave tails of these peaks (Helms et al. 2008; Grunert et al 2018). See Section 1.3.1.1 for more details.

Water itself absorbs very strongly, especially outside of the visible region (Figure 1.1), so bio-optical models primarily focus on the wavelength region between ~ 400 and ~ 800 nm. However, even in this wavelength region water is among the darkest surfaces on Earth, which makes it a challenging target to observe remotely and points to the importance of accurate correction of both atmospheric effects and water surface reflections to isolate $R_{rs}(\lambda)$ from the mixed signal at a remote sensor. See Sections 1.3.2 for more details.

Bio-optical models can be broadly categorized into empirical and analytical models with different gradations between the two (see Odermatt et al. (2012) and Ogashawara (2015) for details). Empirical models statistically relate AOPs to concentrations of optically active water constituents whereas analytical models use physical principles of radiative transfer to connect AOPs to the IOPs of the optically-active constituents to estimate their concentrations.

1.3 Model description

The main source of inspiration for the WaterQuality algorithms is the Water Color Simulator (WASI, Gege 2004), a free program for simulation and inversion of water spectra or remote sensing images (WASI-2D, Gege 2014).

Observed above-water hemispherical-directional reflectance $r_{rs}(\lambda)$ is modeled as the sum of remote sensing reflectance $R_{rs}(\lambda)$ and the reflectance of ambient sky and sunlight at the water surface $R_{rs}^{surf}(\lambda)$ as:

$$r_{rs}(\lambda) = R_{rs}(\lambda) + R_{rs}^{surf}(\lambda) \quad (2)$$

Here $R_{rs}(\lambda)$ is modelled with a bio-optical model and $R_{rs}^{surf}(\lambda)$ is modelled with a surface reflectance model.

1.3.1 Bio-optical model

The semi-analytical bio-optical model of Albert and Mobley (2003) for optically deep and shallow water is based on simulations with the program HydroLight (Mobley et al. 1993). In contrast to the similar model by Lee et al. (Lee et al. 1998, 1999), the Albert and Mobley model accounts for variations in sun zenith and viewing angle and covers a wider range of environmental parameters (Göritz et al. 2018).

1.3.1.1 Absorption

Absorption is modeled as the sum of the absorption of pure water and the water constituents:

$$a(\lambda) = \left[a_w(\lambda) + (T - T_0) \frac{da_w(\lambda)}{dT} \right] + a_{wc}(\lambda) \quad (3)$$

with $a_w(\lambda)$ being the absorption coefficient of pure water at a reference temperature ($T_0 = 20^\circ\text{C}$) compiled from different sources¹, $da_w(\lambda)/dT$ (Röttgers et al. 2013) being the temperature gradient, and T being the actual temperature. Both spectra are provided from WASI6 (Gege 2021) and are included in the WaterQuality python package.

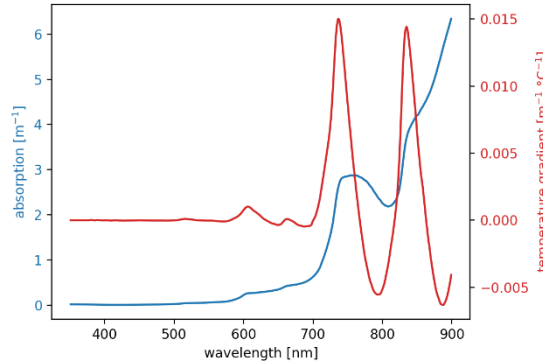


Figure 1.1. Pure water absorption coefficient (blue) and temperature gradient (red).

$a_{wc}(\lambda)$ in Equation 4 is the combined absorption of CDOM, phytoplankton, and non-algal particles (NAP):

$$a_{wc} = a_{CDOM} + a_{phy} + a_{NAP} \quad (4)$$

a_{CDOM} is described by the commonly used exponential approximation for wavelengths greater than 300 nm (Giardino et al. 2019):

$$a_{CDOM}(\lambda) = C_Y * \exp \{-S * (\lambda - \lambda_0)\} \quad (5)$$

where C_Y is CDOM absorption at a reference wavelength λ_0 and S being the spectral slope parameter. The default values are $\lambda_0 = 440 \text{ nm}$ and $S = 0.014 \text{ nm}^{-1}$ (Figure 1.2).

¹ See WASI6 user manual (Gege 2021) for details.

a_{phy} can be modelled as a mixture of up to six different phytoplankton classes through different specific absorption coefficients:

$$a_{phy}(\lambda) = \sum_{i=0}^5 C_i * a_i^*(\lambda) \quad (6)$$

where C_i is the concentration of Chl a in phytoplankton type i , and $a_i^*(\lambda)$ is the mass-specific specific spectral absorption coefficient for phytoplankton type i . The total phytoplankton concentration C_{phy} is the sum of Chl a concentration in all six classes. Commonly, phytoplankton can be reasonably well approximated by a single type. In this case, concentrations of the other classes are set to zero. The six specific absorption coefficients used here were provided by WASI6 (Figure 1.2; Gege 2021, see Section 2.1 for details).

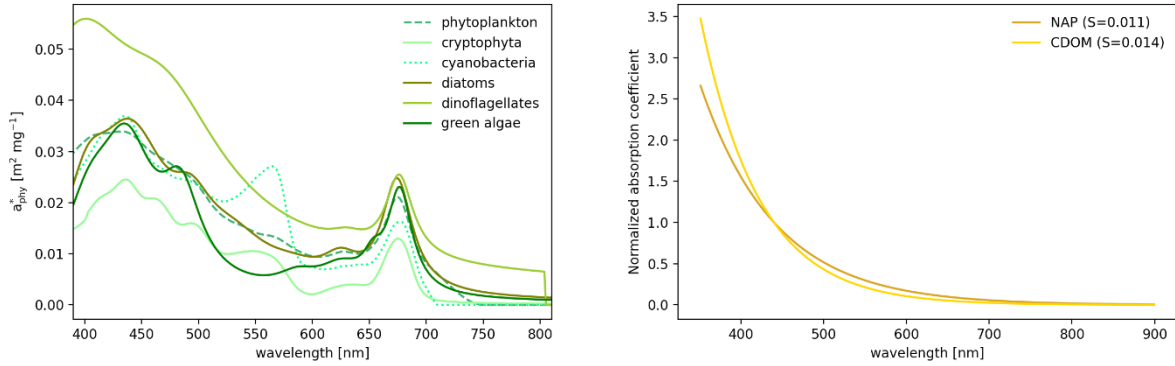


Figure 1.2. Specific absorption coefficients of six phytoplankton types (left) and absorption coefficients of CDOM and NAP normalized at 440 nm (right).

The absorption of NAP is calculated as:

$$a_{NAP} = C_{NAP} * a_{NAP}^*(\lambda_0) * a_{NAP}^N(\lambda) \quad (7)$$

where $a_{NAP}^*(\lambda_0)$ is the specific absorption coefficient of NAP at a reference wavelength λ_0 , $a_{NAP}^N(\lambda)$ is the normalized spectral absorption coefficient of NAP, and C_{NAP} is the concentration of NAP. Here, we use $a_{NAP}^*(440) = 0.041 \text{ m}^2 \text{g}^{-1}$ as given in WASI6. The concentration of NAP is the sum of the concentration of two types of particles with different backscattering properties $C_{NAP} = C_X + C_{Mie}$ which will be further described in Section 1.3.1.2. $a_{NAP}^N(\lambda)$ is approximated as:

$$a_{NAP}^N(\lambda) = \exp\{-S_{NAP} * (\lambda - \lambda_0)\} \quad (8)$$

using $\lambda_0 = 440 \text{ nm}$ and $S_{NAP} = 0.011 \text{ nm}^{-1}$ per default (Figure 1.2). Gege (2021) notes that both, $a_{NAP}^N(\lambda)$ and $a_{NAP}^*(\lambda_0)$, can strongly differ seasonally and regionally, and recommends replacing the approximated default values with regional information if possible.

1.3.1.2 Backscattering

Backscattering is modeled as the sum of the backscattering of pure water and the water constituents:

$$b_b(\lambda) = b_{b,w}(\lambda) + b_{b,phy}(\lambda) + b_{b,NAP}(\lambda) \quad (9)$$

The backscattering coefficient of pure water $b_{b,w}$ is computed using the empirical formula by Morel (1974):

$$b_{b,w} = b_1 * \left(\frac{\lambda}{\lambda_1}\right)^{-4.32} \quad (10)$$

where b_1 depends on salinity and ranges between 0.00111 m^{-1} for fresh water and 0.00144 m^{-1} for oceanic water with a salinity between of 35 and 38‰, and $\lambda_1 = 500 \text{ nm}$.

Backscattering of phytoplankton is computed as:

$$b_{b,phy} = C_{phy} * b_{b,phy}^* * b_{b,phy}^N(\lambda) \quad (11)$$

where C_{phy} is the concentration of phytoplankton (see Section 1.3.1.1). The normalized backscattering coefficient of phytoplankton $b_{b,phy}^N(\lambda)$ (Figure 1.3) is from WASI6² and the specific backscattering coefficient of $b_{b,phy}^*$ at the reference wavelength $\lambda_s = 550 \text{ nm}$ is the default value ($0.0010 \text{ m}^2 \text{ mg}^{-1}$).

The backscattering of NAP is described as a mixture of two spectrally different backscattering coefficients:

$$b_{b,NAP}(\lambda) = [C_X * b_{b,X}^* * b_{b,X}^N(\lambda)] + \left[C_{Mie} * b_{b,Mie} * \left(\frac{\lambda}{\lambda_s}\right)^n \right] \quad (12)$$

Particles of Type I (denoted $_X$) are characterized by arbitrary wavelength dependency of the normalized scattering coefficient, $b_{b,X}^N(\lambda) = 1$, and the specific backscattering coefficient $b_{b,X}^*$ is treated as a constant with a default value of $0.0086 \text{ m}^2 \text{ g}^{-1}$ (Heege 2000, Gege 2021). Particles of Type II (denoted $_{Mie}$) are characterized by the normalized backscattering coefficient $(\lambda / \lambda_s)^n$, with n being related to particle size distribution. Default parameters³ are adopted from WASI6: $b_{b,Mie} = 0.042 \text{ m}^2 \text{ g}^{-1}$, $\lambda_s = 500 \text{ nm}$, and $n = -1$. C_X and C_{Mie} are the concentrations of the respective NAP components in units of mg L^{-1} .

² “The spectrum $b_{b,phy}^N(\lambda)$ provided with WASI was obtained by fitting a measurement of $b_{b,phy}(\lambda)$ for green algae from Lake Garda in the range from 400 to 900 nm (C. Giardino, personal communication) and extrapolating the fit curve to the range from 350 to 1000 nm” (Gege 2021).

³ Representative for Lake Constance (Heege 2000).

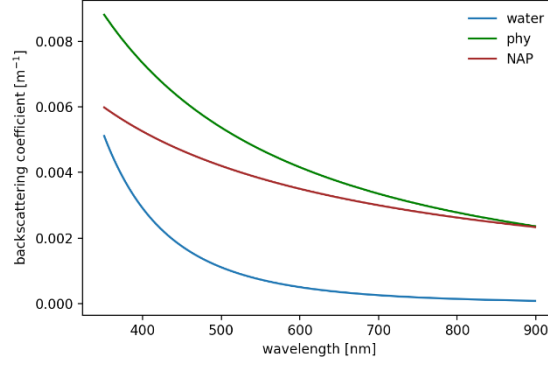


Figure 1.3. Typical backscattering coefficients of water, phytoplankton and NAP. $C_{phy} = 5 \text{ mg m}^{-3}$, $b_{b,phy}^*(550) = 0.001 \text{ m}^2 \text{ mg}^{-1}$, $C_{Mie} = 1 \text{ g m}^{-3}$, $b_{b,Mie}^*(500) = 0.0042 \text{ m}^2 \text{ g}^{-1}$, $n = -1$.

1.3.1.3 Bottom reflectance

Bottom or benthic radiance reflectance $R_{rs}^b(\lambda)$ is modeled as the sum of the relative contribution of up to 6 spectral endmembers:

$$R_{rs}^b(\lambda) = \sum_{n=0}^{N-1} f_n * B_n * a_n(\lambda) \quad (13)$$

where f_n , B_n , and $a_n(\lambda)$ are the areal fraction, the proportion of radiation reflected into the sensor's field of view, and the irradiance reflectance or albedo of bottom type n , respectively. The n bottom types included here (Figure 1.4) represent the following endmembers: (1) a constant reflectance of 10%, (2) sand, (3) coral, (4) crustose coralline algae (CCA), (5) macroalgae, and (6) seagrass. Spectra 2-5 are based on field measurements (Greg Asner, personal communication), which were averaged by class and smoothed using a Savitzky-Golay filter (Savitzky & Golay 1964) with a window length of 45 and a 5th order polynomial. The default is $B_n = \frac{1}{\pi}$ representing isotropic reflectance.

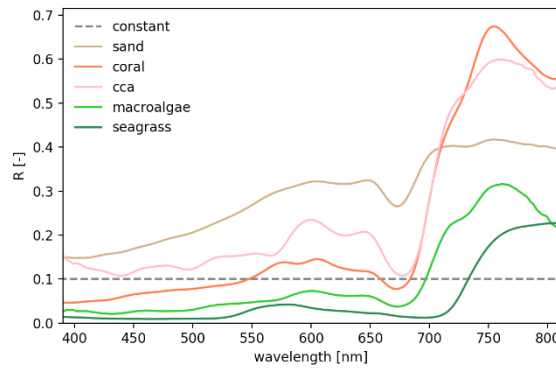


Figure 1.4. Albedo of six bottom types.

1.3.1.4 Diffuse attenuation coefficient of downwelling irradiance

The diffuse attenuation coefficient of downwelling irradiance is computed according to the frequently used approximation implemented in WASI6 (Gege 2021):

$$K_d(\lambda) = \kappa_0 \frac{a(\lambda) + b_b(\lambda)}{\cos \theta'_{sun}} \quad (14)$$

where θ'_{sun} is the sun zenith angle in water computed using Snell's law, the coefficient $\kappa_0 = 1.0546$ per default after Albert and Mobley (2003), $a(\lambda)$ is as defined in Equation 3, and $b_b(\lambda)$ is as defined in Equation 9.

1.3.1.5 Attenuation coefficients of upwelling radiance

To account for differences in the angular distribution of light backscattering in water compared to light reflected from the bottom, diffuse attenuation coefficients of upwelling radiance for water (k_{uW}) and bottom (k_{uB}) are computed separately and according to Albert & Mobley (2003) as:

$$k_{uW}(\lambda) = \frac{a(\lambda) + b_b(\lambda)}{\cos \theta'_v} * (1 + \omega_b(\lambda))^{3.5421} * \left(1 - \frac{0.2786}{\cos \theta'_{sun}}\right) \quad (15)$$

$$k_{uB}(\lambda) = \frac{a(\lambda) + b_b(\lambda)}{\cos \theta'_v} * (1 + \omega_b(\lambda))^{2.2658} * \left(1 + \frac{0.0577}{\cos \theta'_{sun}}\right) \quad (16)$$

where θ'_v is the viewing angle in water computed using Snell's law and $\omega_b(\lambda)$ is defined as:

$$\omega_b(\lambda) = \frac{b_b(\lambda)}{a(\lambda) + b_b(\lambda)} \quad (17)$$

1.3.1.6 Subsurface radiance reflectance and remote sensing reflectance

Subsurface radiance reflectance of deep water is computed as:

$$r_{rs}^{deep-}(\lambda) = f_{rs} * \omega_b(\lambda) \quad (18)$$

where:

$$f_{rs}(\lambda) = 0.0512 * (1 + 4.6659 * \omega_b(\lambda) - 7.8387 * \omega_b(\lambda)^2 + 5.4571 * \omega_b(\lambda)^3) * \left(1 + \frac{0.1098}{\cos \theta'_{sun}}\right) * \left(1 + \frac{0.4021}{\cos \theta'_v}\right) \quad (19)$$

Subsurface radiance reflectance of shallow water is defined as:

$$r_{rs}^{sh-} = r_{rs}^{deep-} * [1 - A_{rs,1} * \exp\{-(K_d(\lambda) + k_{uW}(\lambda)) * zB\}] + A_{rs,2} * R_{rs}^b(\lambda) * \exp\{-(K_d(\lambda) + k_{uB}(\lambda)) * zB\} \quad (20)$$

where zB is water depth, and the empirical constants are defined after Albert & Mobley (2003) as $A_{rs,1} = 1.1576$ and $A_{rs,2} = 1.0389$.

Finally, $R_{rs}(\lambda)$ is related to $r_{rs}^-(\lambda)$ following Lee (1998):

$$R_{rs}(\lambda) = \frac{\zeta * r_{rs}^-(\lambda)}{1 - \Gamma * r_{rs}^-(\lambda)} \quad (21)$$

where $\Gamma \approx 1.6$ and $\zeta \approx 0.52$ (Giardino et al. 2019).

1.3.2 Surface reflectance model

Because a downward pointing sensor above the water surface will always measure not only the signal of the water body but also reflections of the ambient light field at the water surface (i.e., glint), these effects must be corrected for. We implemented a model to correct for sky and sun glint first described in Gege (2012) that builds on the model by Gregg and Carder (1990), and coupled that model to the bio-optical model by Albert & Mobley (2003) described in Section 1.3.1 (see Equation 2).

Surface reflectance R_{rs}^{surf} is defined as:

$$R_{rs}^{surf}(\lambda) = \rho_L * \frac{L_s(\lambda)}{E_d(\lambda)} \quad (22)$$

where ρ_L is the fraction of sky radiance $L_s(\lambda)$ ⁴ that is reflected from the water surface into the sensor's FOV (for viewing angles close to nadir $\rho_L \approx 0.02$) and $E_d(\lambda)$ is downwelling irradiance.

Following Gege (2021), $E_d(\lambda)$ is split into a direct component $E_{dd}(\lambda)$ and a diffuse component $E_{ds}(\lambda)$:

$$E_d(\lambda) = f_{dd} * E_{dd}(\lambda) + f_{ds} * E_{ds}(\lambda) \quad (23)$$

where f_{dd} and f_{ds} are the intensities of the different light sources and $E_{ds}(\lambda)$ is described as the sum of aerosol scattering $E_{dsa}(\lambda)$ and Rayleigh scattering $E_{dsr}(\lambda)$:

$$E_{ds}(\lambda) = E_{dsr}(\lambda) + E_{dsa}(\lambda) \quad (24)$$

Following Gege (2012, 2021), the three components of $E_d(\lambda)$ are calculated as:

$$E_{dd}(\lambda) = E_0(\lambda) \cos\theta_{sun} T_r(\lambda) T_{aa}(\lambda) T_{as}(\lambda) T_{oz}(\lambda) T_{ox}(\lambda) T_{wv}(\lambda) \quad (25)$$

$$E_{dsr}(\lambda) = 0.5 E_0(\lambda) \cos\theta_{sun} (1 - T_r(\lambda)^{0.95}) T_{aa}(\lambda) T_{oz}(\lambda) T_{ox}(\lambda) T_{wv}(\lambda) \quad (26)$$

$$E_{dsa}(\lambda) = E_0(\lambda) \cos\theta_{sun} (T_r(\lambda)^{1.5}) T_{aa}(\lambda) T_{oz}(\lambda) T_{ox}(\lambda) T_{wv}(\lambda) (1 - T_{as}(\lambda)) F_a \quad (27)$$

⁴ $L_s(\lambda)$ does not represent a “piece of sky” at a specific zenith and azimuth angle but is an adaptation in WASI to model radiance reflected at a water surface which is not perfectly flat (Gege 2021).

where $E_0(\lambda)$ is the extraterrestrial solar irradiance corrected for earth–sun distance and orbital eccentricity, and θ_{sun} and F_a are the solar zenith angle and the aerosol forward scattering probability, respectively. The T functions describe atmospheric transmittance after scattering and absorption of the respective components (T_r : Rayleigh scattering, T_{aa} : aerosol absorption, T_{as} : aerosol scattering, T_{oz} : ozone absorption, T_{ox} : oxygen absorption, T_{wv} : water vapor absorption) and are computed following Gege (2012):

$$T_r(\lambda) = \exp[-M'/(115.6406\lambda^4 - 1.335\lambda^2)] \quad (28)$$

$$T_{aa}(\lambda) = \exp[-(1 - \omega_a)\tau_a(\lambda)M] \quad (29)$$

$$T_{as}(\lambda) = \exp[-\omega_a\tau_a(\lambda)M] \quad (30)$$

$$T_{oz}(\lambda) = \exp[-a_{oz}(\lambda)H_{oz}M_{oz}] \quad (31)$$

$$T_{ox}(\lambda) = \exp \frac{-1.41a_{ox}(\lambda) * M'}{[1 + 118.3a_{ox}(\lambda) * M']^{0.45}} \quad (32)$$

$$T_{wv}(\lambda) = \exp \frac{-0.2385a_{wv}(\lambda)WV * M}{[1 + 20.07a_{wv}(\lambda)WV * M]^{0.45}} \quad (33)$$

where atmospheric path length $M = 1/[\cos\theta_{sun} + a(90^\circ + b - \theta_{sun})^{-c}]$, with $a = 0.25, b = 3.885^\circ, c = 1.253$, path length corrected for atmospheric pressure $M' = M * P/(1013.35 \text{ mbar})$, with P being the actual pressure, and ozone path length $M_{oz} = 1.0035 / (\cos^2 \theta_{sun} + 0.007)^{0.5}$.

Aerosol characteristics are defined by aerosol optical thickness $\tau_a = \beta * (\lambda/\lambda_a)^{-\alpha}$ where α is the Ångström exponent and β is a measure of concentration, and aerosol single scattering albedo $\omega_a = (-0.0032AM + 0.972) * \exp(3.06 * 10^{-4}RH)$ where AM is air mass type (ranging from 1 for open ocean aerosols to 10 for continental aerosol) and RH is relative humidity in %. Default values are $\alpha = 1.317$, $\beta = 0.2606$, $AM = 5$, $RH = 80$, $\lambda_a = 550 \text{ nm}$. Alternatively, β can be computed based on aerosol scale height H_a and horizontal visibility V as $\beta = 3.91 * \frac{H_a}{V}$. Aerosol forward scattering probability is defined as:

$$F_a = 1 - 0.5 \exp[(B_1 + B_2 \cos\theta_{sun}) * \cos\theta_{sun}] \quad (34)$$

where $B_1 = B_3[1.459 + B_3(0.1595 + 0.4129 B_3)]$, $B_2 = B_3[0.0783 + B_3(-0.3824 - 0.5874 B_3)]$, $B_3 = \ln(1 - \langle \cos\theta_{sun} \rangle)$, and $\langle \cos\theta_{sun} \rangle = -0.1417\alpha + 0.82$. WV is water vapor concentration in precipitable units (default: $WV = 2.5 \text{ cm}$), H_{oz} is ozone scale height (default: $H_{oz} = 0.38 \text{ cm}$). The absorption spectra a_{wv} , a_{oz} and a_{ox} are read from file and were generated using MODTRAN-3 (Gege 2012).

Sky radiance $L_s(\lambda)$ is calculated as:

$$L_s(\lambda) = g_{dd} * E_{dd}(\lambda) + g_{dsr} * E_{dsr}(\lambda) + g_{dsa} * E_{dsa}(\lambda) \quad (35)$$

Where the g_d parameters are the intensities of the $E_d(\lambda)$ components in units of sr^{-1} .

1.3.3 Model inversion

The model described in Sections 1.3.1 and 1.3.2 is used to retrieve fitted parameters from measured spectra by inversion through non-linear least-squares minimization of the absolute differences (AD) between a measured and a simulated spectrum, using the Trust Region Reflective method (Branch et al. 1999):

$$AD = \sum_i^i |(r_{rs}(\lambda_i) - r_{rs}^{sim}(\lambda_i))| * W(\lambda_i) \quad (36)$$

Where $W(\lambda_i)$ is a spectral weighting coefficient per band i (default: constant $W(\lambda_i) = 1$). The model is initiated with pre-defined start values and stops if an optimal solution has been found or after a pre-defined number of maximum iterations.

1.4 Assumptions and Limitations

Due to the high complexity of coastal, shallow, and inland waters, remote sensing of these environments is not yet considered operational. Except for some regional processors that incorporate site-specific knowledge, generic algorithms do not produce reliable results (Palmer et al 2015; Gege 2017). Here we describe some of the major underlying challenges.

Pure water pixel assumption

The model described here assumes that spectra represent water (i.e. no fractional cover of land) without any build up of materials at the water surface such as floating debris or macroalgae, whitecaps, or algal scum.

Atmospheric correction

Atmospheric correction (AC) is a critical step in the processing of optical remote sensing data and especially for water applications in coastal environments. Water surfaces are highly absorbing and among the darkest features of the Earth's surface. The low reflectance of water results in a relatively strong contribution of atmospheric effects (in the order of 99%) to the total radiance signal received at a satellite sensor (Giardino et al. 2019). Thus, the impact of AC residuals has a strong impact on the shape and intensity of reflectance at the bottom of the atmosphere (BOA) and eventually on the retrieval of water quality parameters. AC for coastal and inland waters is particularly challenging because of (1) the heterogeneous atmospheric conditions resulting from a mixture of terrestrial and maritime influences, and (2) adjacency effects of terrestrial surfaces contributing to the total at-sensor radiance. In addition, (3) non-negligible reflectance of sediment-rich coastal waters in the NIR contradicts AC schemes designed for open ocean applications (Giardino et al. 2019). AC quality therefore may heavily impact the ability of bio-optical models to quantify concentrations of water constituents.

Spectral variability

Spectral libraries (e.g., the mass-specific absorption coefficients of different phytoplankton types or the albedos of different bottom types) can only represent a portion of the spatio-temporal variability existing in nature (Gege 2017). Although the models of Albert and Mobley (2003) and Gege (2012) are physics-based, certain IOPs rely on measurements, which may not be adequate for all environmental conditions (Giardino et al. 2019). Additionally, the algorithm inherent IOP models (e.g., the functional forms used for a_{CDOM} or a_{NAP}) are well established and suitable in many situations but are nevertheless simplifications that may not adequately characterize their respective components (Gege 2017).

Spectral ambiguities

The variety of components and specific IOPs presents a significant numerical challenge for inversion because various combinations of water constituents can result in similar reflectance spectra (Defion-Platel & Chami 2007). This problem can be handled through constraining ranges and interactions of parameters but requires site-specific knowledge (Gege 2017). This problem is particularly relevant for optically shallow waters compared to optically deep waters because inversion requires fitting additional parameters (e.g. depth, bottom types) and thus may hamper the retrieval of target model parameters.

Masking effect

Relatively high abundance of one or more components may mask effects of other less abundant ones. For example, high CDOM may mask effects of Chl *a* concentrations on water reflectance, and thus, hampers retrieval of the latter (Giardino et al. 2019).

Vertical homogeneity

Commonly, bio-optical models assume optically active constituents to be homogeneously distributed in a well-mixed water column. Yet, cyanobacteria are known to actively change their position in the water column (Kutser 2008), and differences in water density can cause stratification of water bodies into layers with different IOPs (Kutser 2004). Because the penetration depth of light into water is wavelength dependent, the resulting reflectance spectra may influence estimation accuracy of bio-optical models.

Inelastic processes

The bio-optical model described in Sec. 1.3 does neither account for Raman scattering nor for sun-induced fluorescence signals from Chl *a*, phycobiliproteins, phaeopigments and CDOM, which may result in relatively large residuals between measured and fit spectra at affected wavelength regions if concentrations of the corresponding sources of fluorescence are high (Lee 1999, Albert & Mobley 2003).

Map grid cell size

The scalability of certain phenomena depends on their local variance, relative to the spatial resolution (Woodcock and Strahler, 1987). Water quality parameters usually change on the scale of tens or hundreds of meters (Powell et al. 1975; Moses et al. 2016). In optically shallow waters, however, bottom coverage may change on smaller spatial scales (e.g., in patchy seagrass meadows or in coral reefs), which may challenge mapping of different bottom type classes if spatial resolution is large compared to the spectral complexity of the bottom substrate. Tidal currents, resuspension, and biological activity can also create highly dynamic and patchy conditions that lead to underestimation of biogeochemical properties at relatively coarse spatial resolutions (e.g. Figures 3.5–3.7).

2. Technical Details

The WaterQuality GitHub repository⁵ contains the water_quality python package and an iPython notebook that includes example code for how to run the inversion model on extracted spectra from GAO imagery.

2.1 Key Dependencies

The Python version used is 3.7.13; Table 2.1.1 lists information about the used packages.

Table 2.1.1. Used python packages.

Package	Version	Documentation	Repository	License
numpy	1.21.5	https://numpy.org/doc/1.21/index.html	https://github.com/numpy/numpy	BSD-3-Clause license
lmfit	1.0.3	https://lmfit.github.io/lmfit-py/	https://github.com/lmfit/lmfit-py/	BSD-3-Clause license
pandas	1.3.5	https://pandas.pydata.org/pandas-docs/version/1.3/index.html	https://github.com/pandas-dev/pandas	BSD-3-Clause license
scikit-learn	1.0.2	https://scikit-learn.org/stable/index.html	https://github.com/scikit-learn/scikit-learn	BSD-3-Clause license
Spectral Python	0.22.4	http://www.spectralpython.net/	https://github.com/spectralpython/spectral	MIT

2.2 Repository structure

The model described in Section 1.3 has been translated into the water_quality python package which is structured in five modules and one data folder (Figure 2.1). The atmosphere module contains all functions to describe the atmospheric processes described in Section 1.3.2. The data folder contains spectral libraries for different parts of the model. The helper module contains specific resampling functions for each of the files in the data folder, respectively. The model module contains the model of Albert & Mobley (2003) and combines it with the surface reflectance model of Gege (2012) which is described in the surface module. The water module contains the functions to describe the processes described in Section 1.3.1.

⁵ <https://github.com/CMLandOcean/WaterQuality>

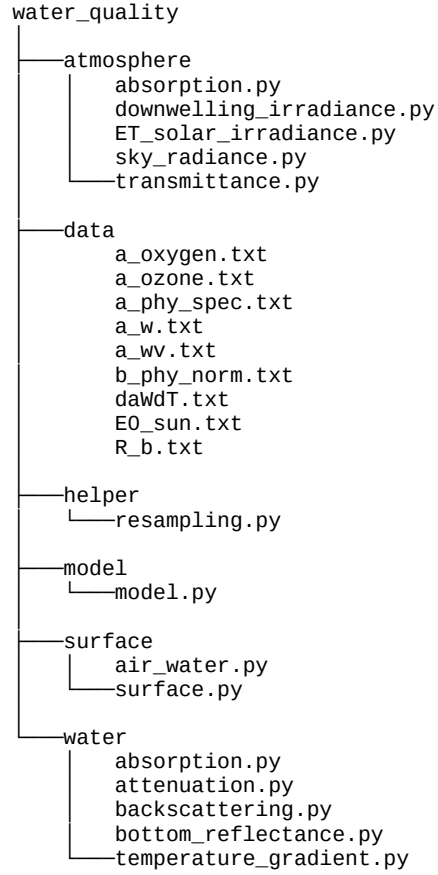


Figure 2.1. Tree diagram of the water_quality python package.

2.2 Input Data Requirements and Algorithm Constraints

Input data must be arrays of BOA $r_{rs}[\text{sr}^{-1}]$ and corresponding wavelengths [nm] and should cover a significant portion of the relevant wavelength region between ~400 nm and ~800 nm. The weights array $W(\lambda_i)$ must have the same length as the wavelengths and r_{rs} arrays.

The algorithm depends on inputs read from file, e.g., the specific absorption coefficients of different phytoplankton types or benthic reflectance classes. Table 2.2.1 describes the spectra read from file, included as text files in the data folder of the GitHub repository.

Table 2.2.1. Spectral library files in the data folder of the GitHub repository.

File name	Description
a_oxygen.txt	Absorption of oxygen
a_ozone.txt	Absorption of ozone
a_phy_spec.txt	Specific absorption of six phytoplankton types
a_w.txt	Absorption of pure water
a_wv.txt	Absorption of water vapor
b_phy_norm.txt	Normalized backscattering coefficient of phytoplankton

dawdT.txt	Temperature gradient of pure water absorption
E0_sun.txt	Extraterrestrial solar irradiance
R_b.txt	Irradiance reflectance of six bottom types

The code is designed in a top-down approach to make use of memoization. For computational reasons, all spectra read from file should be resampled before inversion or simulation using the corresponding functions that build on the `band_resampler()` function from the `spectral` python package. They can then be passed to any appropriate function as input parameters. The same is true for all parts of the model not affected by fitting (depending on the selection of fit parameters). For example, if none of the parameters of $E_d(\lambda)$ is fit, $E_d(\lambda)$ can be precomputed using the corresponding function and passed as an input argument. If not provided, resampling and computation of all parts of the model is performed internally.

The model is inverted through the `inverse()` function that builds on the `minimize()` function from the `lmfit` python package (Newville et al. 2021). All parameters required to specify the model including start, minimum and maximum values, constraints, and selection of fit parameters are defined using an `lmfit.Parameters()` object (see Table 2.2.2 and iPython notebook for details). Some of the parameters are constants and should not be changed by the user (e.g., the reference wavelength for backscattering of pure water or the reference temperature of pure water absorption; see Table 2.2.2). Table 2.2.3 lists adjustable parameters that are not necessarily good fit parameters but can be changed, e.g., in the context of sensitivity analyses. Table 2.2.4 lists adjustable parameters that are typical fit parameters. Note that the number of fit parameters should be kept as small as possible to avoid ambiguities (Defion-Platel & Chami 2007). The user can specify if the bio-optical model or the combination of bio-optical and surface model should be fit using the `'fit_surface'` parameter. The default number of maximum iterations and optimization method are set to 400 and `'least-squares'` by default. As described above, all spectra used in the model which are not affected by the fit process can be passed to the function to speed up inversion. The model can also be used for simulation using the `forward()` function, which requires a `Parameters()` object to specify the model and an array of wavelengths [nm]. Optionally, spectra used in the model can be precomputed and resampled, and then be passed to the function to speed up simulations.

Table 2.2.2. Model constants.

Text symbol	Code symbol	Default	Units	Description
λ_1	lambda_1	500	nm	reference wavelength for backscattering of pure water
λ_s	lambda_S	500	nm	reference wavelength for scattering of particles type II
-	n1	1	-	refractive index of origin medium (air)
-	n2	1.33	-	refractive index of destination medium (water)

κ_0	kappa_0	1.0546	-	coefficient depending on scattering phase function
T_0	T_w_0	20	°C	reference temperature of pure water absorption

Table 2.2.3. Adjustable parameters.

Text symbol	Code symbol	Default	Units	Description
B_i	B_0..B_5	$\frac{1}{\pi}$	sr ⁻¹	proportion of radiation reflected towards the sensor from bottom type i, i=0..5
$b_{b,phy}^*$	b_bphy_spec	0.001	m ² mg ⁻¹	specific backscattering coefficient of phytoplankton at 550 nm
$b_{b,Mie}^*$	b_bMie_spec	0.0042	m ² g ⁻¹	specific backscattering coefficient of non-algal particles type II
$b_{b,X}^*$	b_bX_spec	0.0086	m ² g ⁻¹	specific backscattering coefficient of non-algal particles type I
$b_{b,X}^N$	b_bX_norm_factor	1	-	normalized scattering coefficient of particles type I
$a_{NAP}^*(\lambda_0)$	a_NAP_spec_lambda_0	0.041	m ² g ⁻¹	specific absorption coefficient of NAP at reference wavelength λ_0
S_{NAP}	S_NAP	0.11	nm ⁻¹	exponent of NAP absorption
K	K	0	m ⁻¹	constant added to the CDOM exponential function
n	n	-1	-	Ångström exponent of particle type II backscattering
λ_0	lambda_0	440	nm	reference wavelength for CDOM and NAP absorption
θ_{sun}	theta_sun	np.radians(30)	radians	sun zenith angle in air
θ_v	theta_view	np.radians(0)	radians	viewing angle in air
-	fresh	False	-	boolean to define if $b_{bw}(\lambda)$ is computed for fresh or salt water

T	T_W	20	°C	actual water temperature
P	P	1013.25	mbar	atmospheric pressure
AM	AM	5	-	air mass type
RH	RH	80	%	relative humidity
H_{oz}	H_oz	0.381	cm	ozone scale height
WV	wv	2.5	cm	precipitable water
α	alpha	1.317	-	Ångström exponent of aerosol scattering
β	beta	0.2606	-	turbidity coefficient
f_{dd}	f_dd	1	-	fraction of direct downwelling irradiance
f_{ds}	f_ds	1	-	fraction of diffuse downwelling irradiance
ρ_L	rho_L	0.02	-	reflection factor of downwelling radiance

Table 2.2.4. Typical fit parameters.

Text symbol	Code symbol	Default	Units	Description
C_i	C_0...C_5	0	$\mu\text{g L}^{-1}$	concentration of chlorophyll a in phytoplankton type i, i=0..5
C_Y	C_Y	0	m^{-1}	CDOM absorption coefficient at wavelength λ_0
C_X	C_X	0	mg L^{-1}	concentration of NAP particles type I
C_{Mie}	C_Mie	0	mg L^{-1}	concentration of NAP particles type II

f_i	f_0...f_5	0	-	fraction cover of bottom type number i, i = 0..5
S	s	0.14	nm ⁻¹	exponent of CDOM absorption
g_{dd}	g_dd	0.02	sr ⁻¹	intensity of direct component of downwelling irradiance
g_{dsa}	g_dsa	$\frac{1}{\pi}$	sr ⁻¹	intensity of aerosol scattering part of diffuse component of downwelling irradiance
g_{dsr}	g_dsr	$\frac{1}{\pi}$	sr ⁻¹	intensity of Rayleigh scattering part of diffuse component of downwelling irradiance

2.3 Outputs

The `inverse()` function returns an `MinimizerResult()` object that contains the optimized fit parameters and the fit statistics. The `forward()` function returns an array of $r_{rs}(\lambda)$ for the provided wavelengths.

3. Example Data Set

In January 2023, a field campaign was conducted in Hawai'i to collect a comprehensive comparison data set consisting of relevant field and imaging spectroscopy data collected simultaneously with airborne imaging spectroscopy using the Global Airborne Observatory (GAO).

3.1 Field data

3.1.1 Water sample analysis

Water samples were collected from the top 50 cm of the water column within one hour of GAO overpasses for measurements of Chl, SPM, and CDOM. SPM and Chl a samples were obtained by filtering collected water samples on 0.7 μ m pre-combusted glass fiber filters with a vacuum pump with 24 hours of collection. SPM filter samples were oven-dried and concentration was determined by mass difference. Chl-a filter samples were immediately stored at -80°C after filtration and analyzed on a Trilogy Fluorometer (Turner Designs) after 24 hour acetone extraction. CDOM samples were directly filtered on vessel using sterile 0.2 μ m polyethersulfone filters and filtrate was stored in the dark at 4 °C in pre-combusted amber glass bottles until analysis. CDOM spectral absorption coefficients were measured using a Cary 4000 dual-beam spectrophotometer.

3.1.2 Field spectroscopy

We used an SVC HR-512i spectroradiometer (Spectra Vista Corporation, USA) to conduct above-water radiometric measurements following protocols of the International Ocean Color Coordinating Group (IOCCG; Zibordi et al. 2019). Residual glint was corrected using the model described in section 1.3 by first inverting the measured spectrum and then subtracting the retrieved glint signal (Figure 3.1). The glint corrected spectrum was then compared to GAO data likewise corrected with the same approach to assess atmospheric correction performance (see Section 3.2.1).

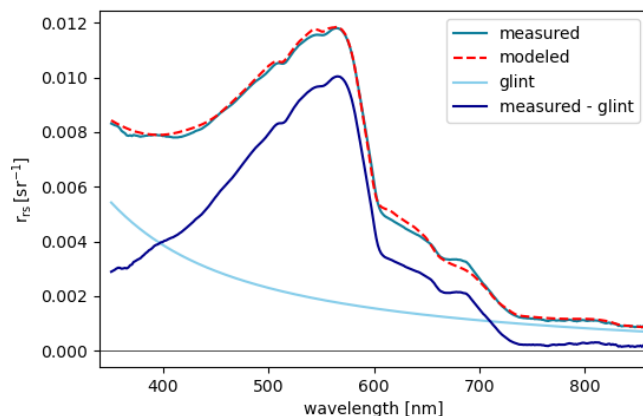


Figure 3.1. Example of glint correction on SVC data.

3.2 Imaging spectroscopy data

3.2.1 Atmospheric correction

GAO VSWIR data were atmospherically corrected with ATREM (ATmospheric REMoval, Gao and Goetz 1990) and the wavelength regions from < 420 nm and > 900 nm were masked, respectively, resulting in 96 remaining bands. As described above, atmospheric correction is a crucial part for the retrieval of water quality parameters from remotely sensed imagery because of the relative low reflectance of water. To assess the atmospheric correction applied to the GAO imagery, we first corrected residual glint by first inverting the atmospherically corrected spectrum⁶, and then subtracting the retrieved glint signal. Figure 3.2 shows examples of both field-based (SVC) and airborne (GAO) spectra after glint correction. Figure 3.3 demonstrates the performance of the glint correction on GAO imagery.

⁶ Fit parameters: C_0, C_X, C_Mie, zB, f_0..f_5, g_dd, g_dsr, g_dsa

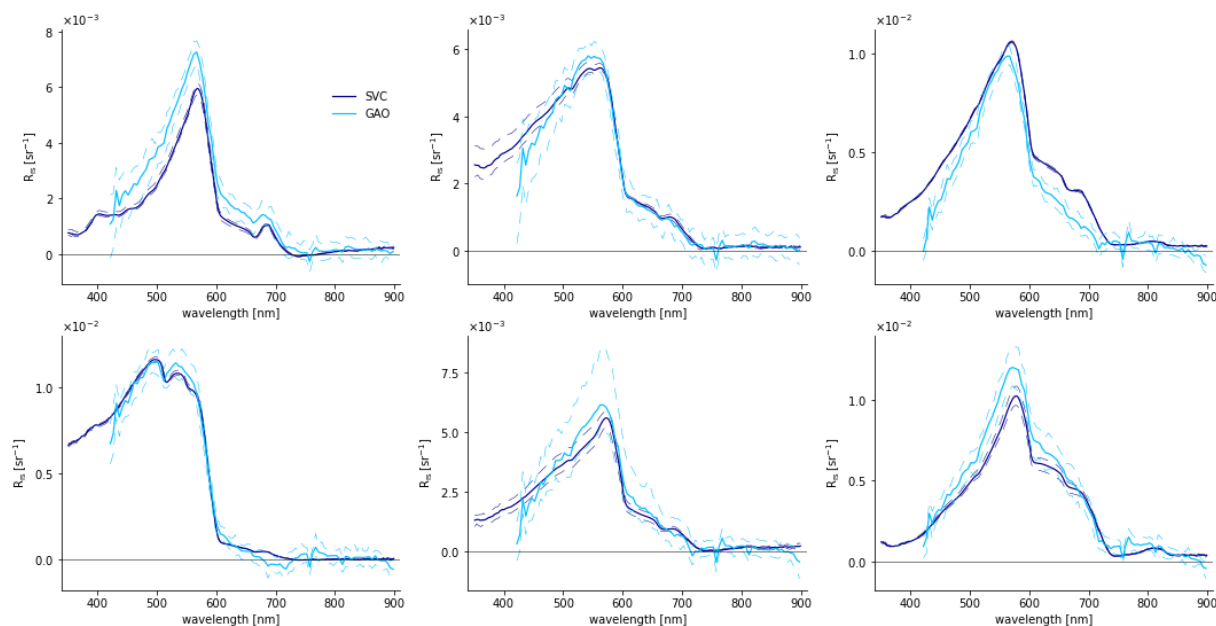


Figure 3.2. Comparison of GAO and SVC spectra after glint correction at selected sites. Solid lines are mean spectra, dashed lines indicate min/max.

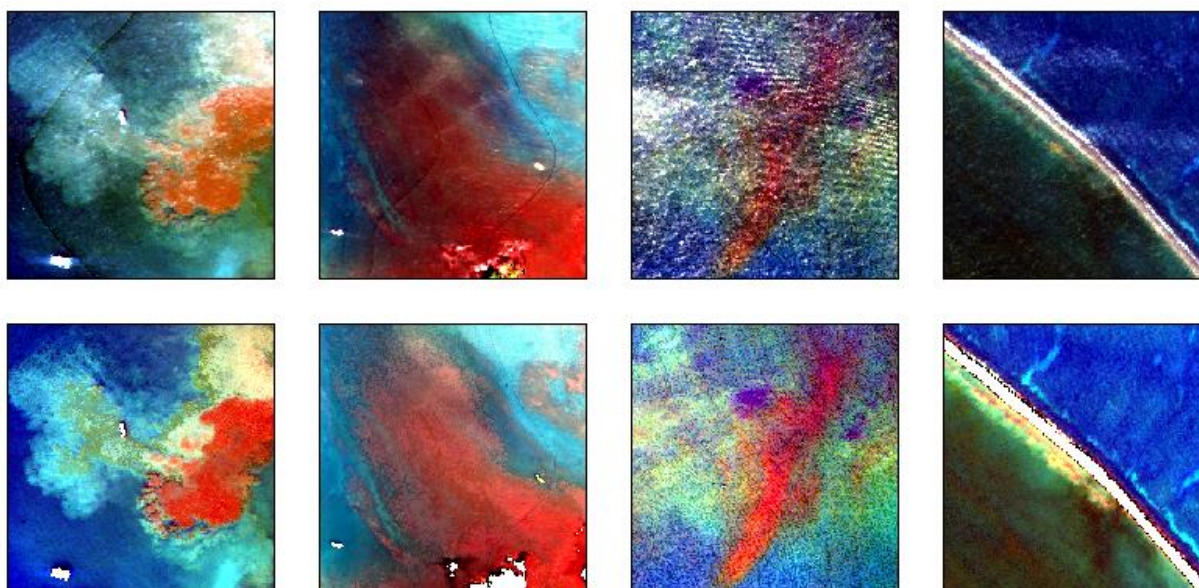


Figure 3.3. Selected 300m x 300m areas of GAO imagery before (top row) and after (bottom row) glint correction and masking of non-water pixels.

3.2.2 Simulated Tanager data

In addition to testing on field spectra and extracted GAO pixels, we also examined the effects of running the WaterQuality algorithm on the GAO VSWIR data modified to mimic data from the upcoming Tanager sensors. For this, we divided the original rawspace GAO VSWIR data into a grid with an

approximate 30m GSD. The X/Y locations, as determined with orthorectification, of all rawspace pixels within each grid cell were averaged to get a center coordinate for the 30 m output pixel. Also within each 30 m output pixel, applied a gaussian mean filter with $\sigma = 30.0 / (2 \sqrt{2 \log 2})$ on the radiance pixel values surrounding each determined output pixel center, with weights determined by individual pixel distance from center in map coordinates. Simulated noise was added to this convolved radiance map using the radiometric model provided by Planet Labs PBC, and these data were processed to reflectance using the same methodology as for the full resolution image.

3.3 Performance Evaluation

After masking all non-water pixels identified with the Automated Water Extraction Index (AWEI; Feyisa et al. 2014), we extracted all GAO spectra from a 5 m buffer around the GPS locations attributed to each water sampling station from the glint corrected flight line closest in time to the field sampling. We then ran only the bio-optical model on the extracted spectra (see Table A.1 for parameter settings), computed the median and standard deviation for the retrieved parameters and compared the median of all pixels to the corresponding median field data from the same station. SPM is computed as the sum of NAP and Chl a:

$$C_{SPM} = C_X + C_{Mie} + C_{phy} \quad (37)$$

For each water quality parameter, we compute accuracy and precision of the proposed retrieval using Pearson's correlation coefficient (r) and the root-mean squared error (RMSE). In addition, we calculated the commonly used coefficient of determination (R^2) between measured and modeled values as well as slope and y-intercept of the line of best fit of the linear regression (Figure 3.4). Figures 3.5–3.7 compare model results at GAO and Tanager scale; Figure 3.8 shows an example simulated Tanager spectrum before and after glint correction.

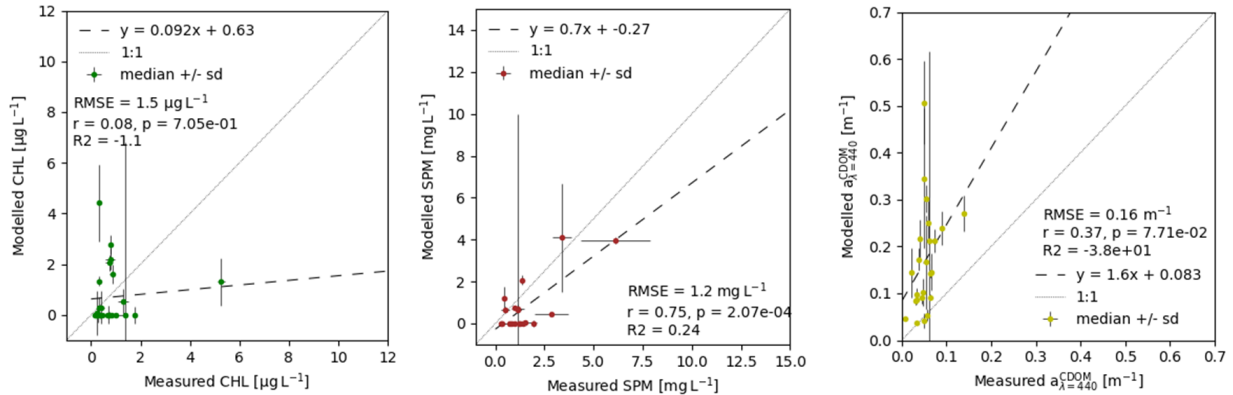


Figure 3.4. Scatter plots of measured vs. simulated water quality parameters.

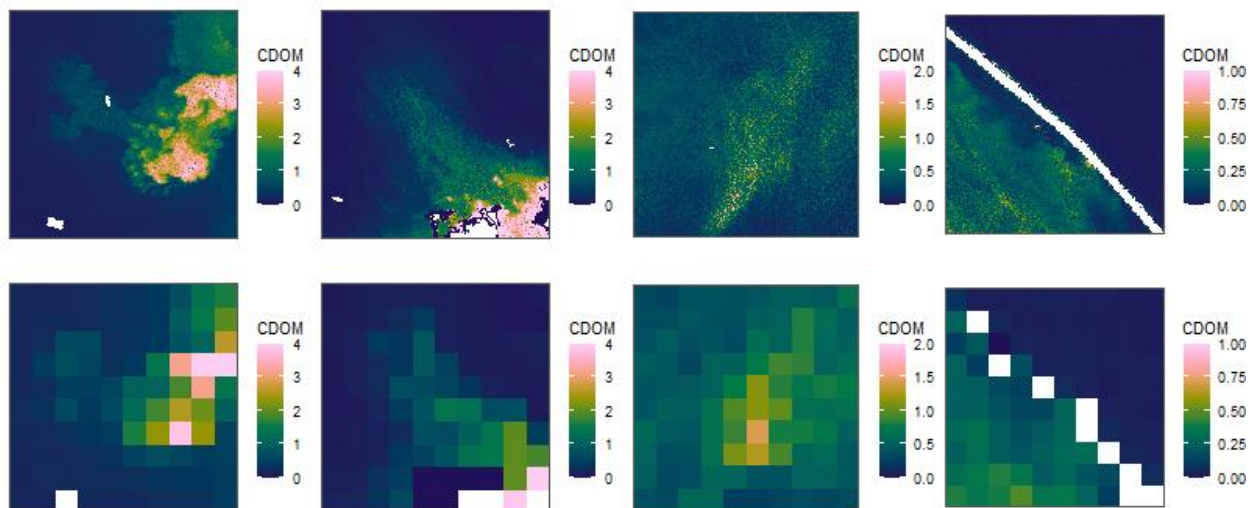


Figure 3.5. Modeled CDOM absorption at 440 nm (m^{-1}) for select 300m x 300m regions at GAO and Tanager scale. Masked pixels (non-water) are shown in white.

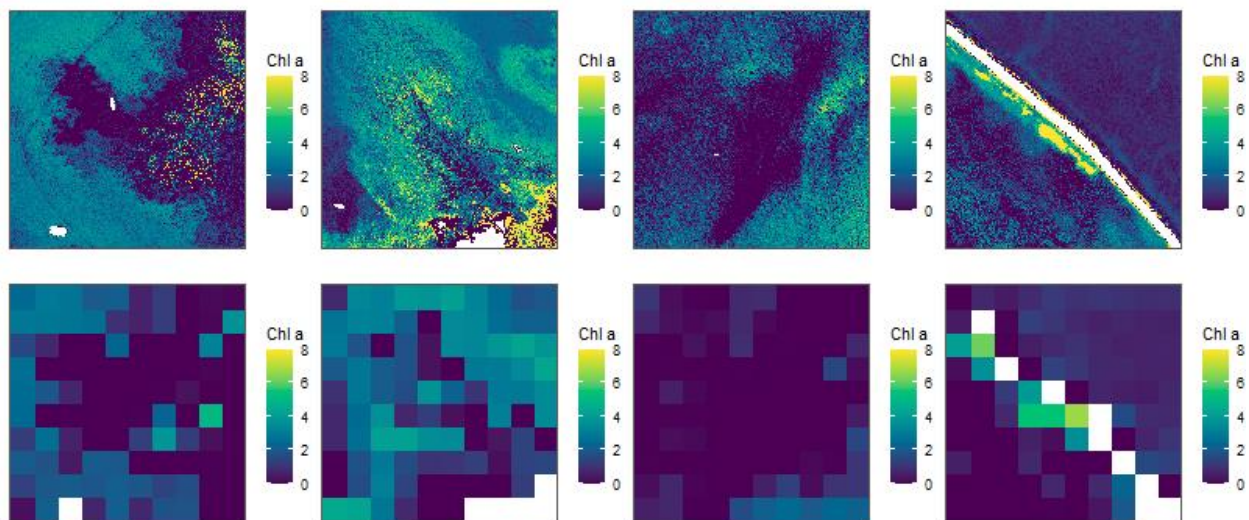


Figure 3.6. Modeled Chl a concentration ($\mu\text{g L}^{-1}$) for select 300m x 300m regions at GAO and Tanager scale. Masked pixels (non-water) are shown in white.

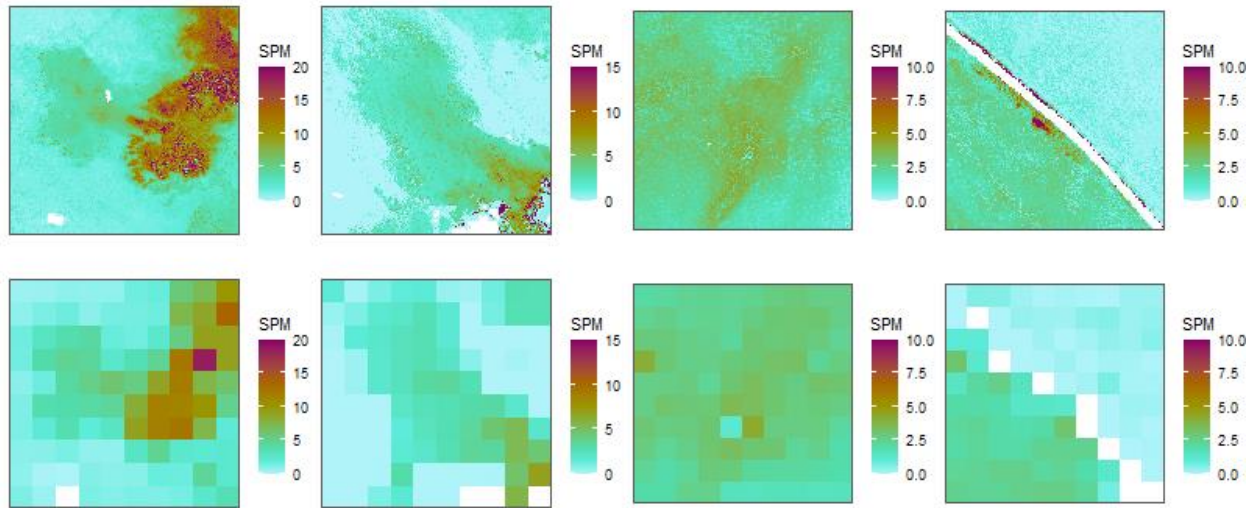


Figure 3.7. Modeled SPM concentration (mg L^{-1}) for select 300m x 300m regions at GAO and Tanager scale. Masked pixels (non-water) are shown in white.

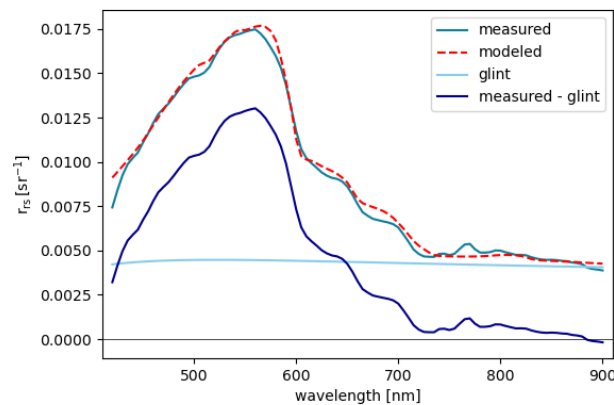


Figure 3.8. Simulated Tanager scale spectrum before and after glint correction.

References

- Albert, A., & Mobley, C. (2003). An analytical model for subsurface irradiance and remote sensing reflectance in deep and shallow case-2 waters. *Optics Express*, 11(22), 2873. <https://doi.org/10.1364/OE.11.002873>
- Branch, M. A., Coleman, T. F., & Li, Y. (1999). A Subspace, Interior, and Conjugate Gradient Method for Large-Scale Bound-Constrained Minimization Problems. *SIAM Journal on Scientific Computing*, 21(1), 1–23. <https://doi.org/10.1137/S1064827595289108>
- Bricaud, A., Claustre, H., Ras, J., & Oubelkheir, K. (2004). Natural variability of phytoplanktonic absorption in oceanic waters: Influence of the size structure of algal populations. *Journal of Geophysical Research: Oceans*, 109(C11). <https://doi.org/10.1029/2004JC002419>

- Defoin-Platel, M., & Chami, M. (2007). How ambiguous is the inverse problem of ocean color in coastal waters? *Journal of Geophysical Research: Oceans*, 112(C3). <https://doi.org/10.1029/2006JC003847>
- Feyisa, G. L., Meilby, H., Fensholt, R., & Proud, S. R. (2014). Automated Water Extraction Index: A new technique for surface water mapping using Landsat imagery. *Remote Sensing of Environment*, 140, 23–35. <https://doi.org/10.1016/j.rse.2013.08.029>
- Gao, B. C., & Goetz, A. F. (1990). Column atmospheric water vapor and vegetation liquid water retrievals from airborne imaging spectrometer data. *Journal of Geophysical Research: Atmospheres*, 95(D4), 3549–3564. <https://doi.org/10.1029/JD095iD04p03549>
- Gege, P. (2004). The water color simulator WASI: an integrating software tool for analysis and simulation of optical in situ spectra. *Computers & Geosciences*, 30(5), 523–532. <https://doi.org/10.1016/j.cageo.2004.03.005>
- Gege, P. (2012). Analytic model for the direct and diffuse components of downwelling spectral irradiance in water. *Applied Optics*, 51(9), 1407. <https://doi.org/10.1364/AO.51.001407>
- Gege, P. (2014). WASI-2D: A software tool for regionally optimized analysis of imaging spectrometer data from deep and shallow waters. *Computers & Geosciences*, 62, 208–215. <https://doi.org/10.1016/j.cageo.2013.07.022>
- Gege, P., & Groetsch, P. (2016). A spectral model for correcting sun glint and sky glint. *Proceedings of Ocean Optics XXIII*.
- Gege, P. (2017). Radiative Transfer Theory for Inland Waters. In *Bio-optical Modeling and Remote Sensing of Inland Waters* (pp. 25–67). Elsevier. <https://doi.org/10.1016/B978-0-12-804644-9.00002-1>
- Gege, P. (2021). The Water Colour Simulator WASI User manual for WASI version 6 (p. 103).
- Giardino, C., Brando, V. E., Gege, P., Pinnel, N., Hochberg, E., Knaeps, E., Reusen, I., Doerffer, R., Bresciani, M., Braga, F., Foerster, S., Champollion, N., & Dekker, A. (2019). Imaging Spectrometry of Inland and Coastal Waters: State of the Art, Achievements and Perspectives. *Surveys in Geophysics*, 40(3), 401–429. <https://doi.org/10.1007/s10712-018-9476-0>
- Göritz, A., Berger, S., Gege, P., Grossart, H.-P., Nejstgaard, J., Riedel, S., Röttgers, R., & Utschig, C. (2018). Retrieval of Water Constituents from Hyperspectral In-Situ Measurements under Variable Cloud Cover—A Case Study at Lake Stechlin (Germany). *Remote Sensing*, 10(2), 181. <https://doi.org/10.3390/rs10020181>
- Gregg, W. W., & Carder, K. L. (1990). A simple spectral solar irradiance model for cloudless maritime atmospheres. *Limnology and Oceanography*, 35(8), 1657–1675. <https://doi.org/10.4319/lo.1990.35.8.1657>
- Groetsch, P. M. M., Gege, P., Simis, S. G. H., Eleveld, M. A., & Peters, S. W. M. (2017). Validation of a spectral correction procedure for sun and sky reflections in above-water reflectance measurements. *Optics Express*, 25(16), A742. <https://doi.org/10.1364/OE.25.00A742>

Grunert, B. K., Mouw, C. B., & Ciochetto, A. B. (2018). Characterizing CDOM spectral variability across diverse regions and spectral ranges. *Global Biogeochemical Cycles*, 32(1), 57-77.

<https://doi.org/10.1002/2017GB005756>

Heege, T. (2000): Flugzeuggestützte Fernerkundung von Wasserinhaltsstoffen am Bodensee. PhD thesis. DLR-Forschungsbericht 2000-40, 134 p.

Helms, J. R., Stubbins, A., Ritchie, J. D., Minor, E. C., Kieber, D. J., & Mopper, K. (2008). Absorption spectral slopes and slope ratios as indicators of molecular weight, source, and photobleaching of chromophoric dissolved organic matter. *Limnology and oceanography*, 53(3), 955-969.

<https://doi.org/10.4319/lo.2008.53.3.0955>

Kutser, T. (2004). Quantitative detection of chlorophyll in cyanobacterial blooms by satellite remote sensing. *Limnology and Oceanography*, 49(6), 2179-2189. <https://doi.org/10.4319/lo.2004.49.6.2179>

Kutser, T., Metsamaa, L., & Dekker, A. G. (2008). Influence of the vertical distribution of cyanobacteria in the water column on the remote sensing signal. *Estuarine, Coastal and Shelf Science*, 78(4), 649–654.

<https://doi.org/10.1016/j.ecss.2008.02.024>

Lee, Z., Carder, K. L., Mobley, C. D., Steward, R. G., & Patch, J. S. (1998). Hyperspectral remote sensing for shallow waters: 1. A semianalytical model. *Applied Optics*, 37(27), 6329.

<https://doi.org/10.1364/ao.37.006329>

Lee, Z., Carder, K. L., Mobley, C. D., Steward, R. G., & Patch, J. S. (1999). Hyperspectral remote sensing for shallow waters: 2. Deriving bottom depths and water properties by optimization. *Applied Optics*, 38(18), 3831. <https://doi.org/10.1364/ao.38.003831>

Lehmann, M. K., Gurlin, D., Pahlevan, N., Alikas, K., Anstee, J., Balasubramanian, S. V., Barbosa, C. C. F., C., B. B., A., B., M., B., Cao, Z. A., Dekker, A. G., Drayson, N., Errera, R. M., Fernandez, V., Fichot, C. G., Gege, P., Claudia, G., Gitelson, A. A., ... Yue, L. (2023). GLORIA - A globally representative hyperspectral in situ dataset for optical sensing of water quality. *Scientific Data*, 10(1), 100.

<https://doi.org/10.1038/s41597-023-01973-y>

Mobley, C. D., Gentili, B., Gordon, H. R., Jin, Z., Kattawar, G. W., Morel, A., Reinersman, P., Stamnes, K., & Stavn, R. H. (1993). Comparison of numerical models for computing underwater light fields. *Applied Optics*, 32(36), 7484. <https://doi.org/10.1364/AO.32.007484>

Morel, A. (1974). Optical properties of pure water and pure Sea water. In N. G. Jerlov & E. Steemann Nielsen (Eds.), *Optical Aspects of Oceanography* (pp. 1–24). Academic Press.

Moses, W. J., Ackleson, S. G., Hair, J. W., Hostetler, C. A., & Miller, W. D. (2016). Spatial scales of optical variability in the coastal ocean: Implications for remote sensing and in situ sampling. *Journal of Geophysical Research: Oceans*, 121(6), 4194–4208. <https://doi.org/10.1002/2016JC011767>

Newville, M., Stensitzki, T., Allen, D. B. ., & Ingargiola, A. (2021). LMFIT: Non-Linear Least-Square Minimization and Curve-Fitting for Python (1.0.3). <https://doi.org/10.581/zenodo.5570790>

- Odermatt, D., Gitelson, A., Brando, V. E., & Schaepman, M. (2012). Review of constituent retrieval in optically deep and complex waters from satellite imagery. In *Remote Sensing of Environment*. <https://doi.org/10.1016/j.rse.2011.11.013>
- Ogashawara, I. (2015). Terminology and classification of bio-optical algorithms. *Remote Sensing Letters*, 6(8), 613–617. <https://doi.org/10.1080/2150704X.2015.1066523>
- Palmer, S. C., Kutser, T., & Hunter, P. D. (2015). Remote sensing of inland waters: Challenges, progress and future directions. *Remote sensing of Environment*, 157, 1-8. <https://doi.org/10.1016/j.rse.2014.09.021>
- Pope, R. M., & Fry, E. S. (1997). Absorption spectrum (380–700 nm) of pure water II Integrating cavity measurements. *Applied Optics*, 36(33), 8710. <https://doi.org/10.1364/AO.36.008710>
- Powell, T. M., Richerson, P. J., Dillon, T. M., Agee, B. A., Dozier, B. J., Godden, D. A., & Myrup, L. O. (1975). Spatial scales of current speed and phytoplankton biomass fluctuations in Lake Tahoe. *Science*, 189(4208), 1088-1090. <https://doi.org/10.1126/science.189.4208.1088>
- Röttgers, R., Doerffer, R., McKee, D., Schönfeld, W. (2013). Pure water spectral absorption, scattering, and real part of refractive index model. Algorithm Theoretical Basis Document. The Water Optical Properties Processor (WOPP). Distribution: Marc Bouvet, ESA/ESRIN, Revision 7, May 2013.
- Savitzky, A., & Golay, M. J. E. (1964). Smoothing and Differentiation of Data by Simplified Least Squares Procedures. *Analytical Chemistry*, 36(8), 1627–1639. <https://doi.org/10.1021/ac60214a047>
- Stramski, D., Babin, M., & Woźniak, S. B. (2007). Variations in the optical properties of terrigenous mineral-rich particulate matter suspended in seawater. *Limnology and Oceanography*, 52(6), 2418-2433. <https://doi.org/10.4319/lo.2007.52.6.2418>
- Woodcock, C. E., & Strahler, A. H. (1987). The factor of scale in remote sensing. *Remote Sensing of Environment*, 21(3), 311–332. [https://doi.org/10.1016/0034-4257\(87\)90015-0](https://doi.org/10.1016/0034-4257(87)90015-0)
- Zibordi, G., Voss, K. J., Johnson, B. C., & Mueller, J. L. (2019). IOCCG Ocean Optics and Biogeochemistry Protocols for Satellite Ocean Colour Sensor Validation. IOCCG Protocol Series, 3. <https://doi.org/10.25607/OBP-691>

Appendix

Table A.1. Fit parameter setting used to compute water quality parameters.

name	value	initial value	min	max	vary
c_0	0.00000000	0	0.00000000	100.000000	True
c_1	0.00000000	0	0.00000000	100.000000	False
c_2	0.00000000	0	0.00000000	100.000000	False
c_3	0.00000000	0	0.00000000	100.000000	False
c_4	0.00000000	0	0.00000000	100.000000	False
c_5	0.00000000	0	0.00000000	100.000000	False
c_Y	0.00000000	0	0.00000000	4.00000000	True
c_X	0.00000000	0	0.00000000	100.000000	True
c_Mie	0.00000000	0	0.00000000	100.000000	True
f_0	0.00000000	0	0.00000000	1.00000000	True
f_1	0.00000000	0	0.00000000	1.00000000	True
f_2	0.00000000	0	0.00000000	1.00000000	True
f_3	0.00000000	0	0.00000000	1.00000000	True
f_4	0.00000000	0	0.00000000	1.00000000	True
f_5	0.00000000	0	0.00000000	1.00000000	True
B_0	0.31830989	1/np.pi	-inf	inf	False
B_1	0.31830989	1/np.pi	-inf	inf	False

B_2	0.31830989	1/np.pi	-inf	inf	False
B_3	0.31830989	1/np.pi	-inf	inf	False
B_4	0.31830989	1/np.pi	-inf	inf	False
B_5	0.31830989	1/np.pi	-inf	inf	False
b_bphy_spec	1.0000e-03	0.001	-inf	inf	False
b_bMie_spec	0.00420000	0.0042	-inf	inf	False
b_bX_spec	0.00860000	0.0086	0.00000000	1.00000000	False
b_bX_norm_factor	1.00000000	1	-inf	inf	False
a_NAP_spec_lambda_0	0.04100000	0.041	0.01000000	0.12000000	False
S	0.01400000	0.014	0.00700000	0.02600000	True
K	0.00000000	0	0.00000000	inf	False
S_NAP	0.01100000	0.011	-inf	inf	False
n	-1.00000000	-1	-1.00000000	0.00000000	False
lambda_0	440.000000	440	-inf	inf	False
lambda_S	500.000000	500	-inf	inf	False
theta_sun	0.69813170	0.69813	0.00000000	1.57079633	False
theta_view	0.00000000	0.0	0.00000000	1.57079633	False
n1	1.00000000	1	-inf	inf	False
n2	1.33000000	1.33	-inf	inf	False
kappa_0	1.05460000	1.0546	-inf	inf	False

fresh	0.00000000	False	-inf	inf	False
zB	10.00000000	10	0.00000000	100.0000000	True
T_W	25.00000000	25	0.00000000	40.00000000	False
T_W_0	20.00000000	20	-inf	inf	False
P	1013.25000	1013.25	-inf	inf	False
AM	1.00000000	1	-inf	inf	False
RH	60.00000000	60	-inf	inf	False
H_oz	0.38000000	0.38	-inf	inf	False
WV	2.50000000	2.5	-inf	inf	False
alpha	1.31700000	1.317	-inf	inf	False
beta	0.26060000	0.2606	-inf	inf	False
g_dd	0.02000000	0.02	-1.00000000	10.00000000	False
g_dsr	0.31830989	1/np.pi	0.00000000	10.00000000	False
g_dsa	0.31830989	1/np.pi	0.00000000	10.00000000	False
f_dd	1.00000000	1	-inf	inf	False
f_ds	1.00000000	1	-inf	inf	False
rho_L	0.02006000	0.02006	-inf	inf	False
offset	0.00000000	0	-0.10000000	0.10000000	False
fit_surface	0.00000000	False	-inf	inf	False